Mapping anisotropic structure formation of soy protein during high-moisture extrusion

Garina, Ekaterina D.; Kuijpers, Sam A.; Gobes, Martijn I.; Sein, Arjen; den Adel, Ruud; Smith, Gregory N.; Sztucki, Michael; Hohlbein, Johannes; Terenzi, Camilla; van Duynhoven, John

DOI
10.1016/j.foodhyd.2025.112037

Publication date
2026

Document Version
Final published version

Published in
Food Hydrocolloids

Citation (APA)
Garina, E. D., Kuijpers, S. A., Gobes, M. I., Sein, A., den Adel, R., Smith, G. N., Sztucki, M., Hohlbein, J., Terenzi, C., van Duynhoven, J., & Bouwman, W. G. (2026). Mapping anisotropic structure formation of soy protein during high-moisture extrusion. *Food Hydrocolloids*, *172*, Article 112037. https://doi.org/10.1016/j.foodhyd.2025.112037

Food Hydrocolloids 172 (2026) 112037

Contents lists available at ScienceDirect

Food Hydrocolloids

journal homepage: www.elsevier.com/locate/foodhyd

Mapping anisotropic structure formation of soy protein during high-moisture extrusion

Ekaterina D. Garina [a,1], Sam A. Kuijpers [b,1], Martijn I. Gobes [b,1], Arjen Sein [c], Ruud den Adel [d], Gregory N. Smith [e], Michael Sztucki [f], Johannes Hohlbein [b,g], Camilla Terenzi [b], John P.M. van Duynhoven [b,d], Wim G. Bouwman [a,*]

[a] Department of Radiation Science and Technology, Delft University of Technology, Mekelweg 15, 2629 JB Delft, The Netherlands
[b] Laboratory of Biophysics, Wageningen University and Research, Stippeneng 4, 6708 WE Wageningen, The Netherlands
[c] dsm-firmenich, Alexander Fleminglaan 1, 2600 MA Delft, The Netherlands
[d] Unilever Global Foods Innovation Centre, Bronland 14, 6708 WH Wageningen, The Netherlands
[e] ISIS Neutron and Muon Source, Science and Technology Facilities Council, Rutherford Appleton Laboratory, Chilton, Oxon OX11 0QX, UK
[f] ESRF, The European Synchrotron Radiation Facility, 71 Avenue des Martyrs, CS40220, 38043 Grenoble Cedex 9, France
[g] Microscopy Research Facility, Wageningen University & Research, Stippeneng 4, 6708 WE Wageningen, The Netherlands

ARTICLE INFO

Dataset link: https://doi.org/10.5286/ISIS.E.RB2369100, https://doi.org/10.5281/zenodo.14651762

Keywords:
Soy proteins
Structure formation
High-moisture extrusion
Multiscale measurements

ABSTRACT

The development of novel plant-based meat alternatives that closely mimic the anisotropic structure of animal meat offers a solution to mitigate the adverse effects of animal meat consumption. The currently most widely adopted production route is shear processing through high-moisture extrusion (HME). The complex structure formation mechanisms that determine the final fibrous texture of extrudates have yet to be fully understood. The main obstacle is the lack of multiscale studies investigating the principles governing structure formation from the nano- to the macro-structural level. This work aims to address this knowledge gap by studying materials, collected after a dead-stop operation of an industrial pilot-plant scale extruder, with multiple characterisation techniques, such as Magnetic Resonance Imaging (MRI) and Small-Angle Scattering (SAS). We demonstrate that the nm- to μm-scale structure is formed already within the extruder barrels, and that sub-mm-scale anisotropy develops within the cooling die. Furthermore, we show that diffuse light reflectance (DR) probes the size and coarseness of the lamellar phase-separated regions.

1. Introduction

It is widely acknowledged that shifting towards plant-based diets is of crucial importance to mitigate the adverse effects of meat consumption on health, environment, and animal welfare (Bonnet et al., 2020; González et al., 2020; He et al., 2020). The development of novel plant-based meat alternatives, which closely mimic the anisotropic structure of animal meat, offers a promising solution without sacrificing the eating experiences that meat-eaters are used to (Andreani et al., 2023).

High-moisture extrusion (HME) is the dominant industrial processing method for producing fibrous meat alternatives from plant proteins in an efficient and scalable manner (Dekkers et al., 2018). The HME process involves the mixing and hydration of plant proteins, followed by thermo-mechanical treatment and subsequent cooling under shear in a cooling die (Cornet et al., 2022). The plant protein ingredients are typically concentrates obtained through industrial fractionation at a large scale. Such concentrates are less refined than isolates and contain significant amounts of carbohydrate fibres that can also contribute to structure formation (Wang et al., 2023).

The formation of fibrous structures during HME is believed to occur at different length scales (Beniwal et al., 2021; van der Sman & van der Goot, 2023; Wittek, Zeiler, et al., 2021), with the alignment of protein aggregates being considered to be the first structuring process occurring at the smallest length scale. For protein aggregates, it is hypothesised that the balance between their growth and breakdown governs the resulting size (van der Sman & van der Goot, 2023). The growth of protein aggregates is believed to occur in the screw sections at temperatures in the range of 90 °C < T < 120 °C. Meanwhile, shear-induced fragmentation is likely to occur in the subsequent sections where T > 120 °C. These aggregates are resistant to further breakdown by shear forces and likely constitute the building blocks for protein

* Corresponding author.
E-mail address: W.G.Bouwman@tudelft.nl (W.G. Bouwman).
[1] These authors contributed equally to this work as co-first authors.

https://doi.org/10.1016/j.foodhyd.2025.112037
Received 27 June 2025; Received in revised form 9 September 2025; Accepted 24 September 2025
Available online 29 September 2025

fibrils. Therefore, protein fibril alignment is expected to occur (Akdogan, 1999) at length scales larger than that of a single protein aggregate. A second structuring process involves phase separation into protein- and water-rich domains, resulting in syneresis. The underlying mechanisms are, however, still under debate. It has been hypothesised (Kaunisto et al., 2024; Sandoval Murillo et al., 2019) that phase separation results from spinodal decomposition, whereas others (van der Sman & van der Goot, 2023) proposed contraction of the cross-linked protein matrix as the underlying cause. A third structuring process occurs when, besides a continuous anisotropic protein phase, a dispersed phase is present. Such a dispersed phase can deform and elongate under shear (Dekkers et al., 2018; Tolstoguzov, 1993). For example, carbohydrate fibres present in industrial plant-protein concentrates can co-align, along the extrusion direction, with the anisotropic protein network (Garina et al., 2024) in high-moisture extrudates.

In the context of the aforementioned hypotheses it is evident that, while HME is an established technology in the food industry, the underlying mechanisms that lead to fibrous structure formation are not yet fully understood. Empirical approaches that attempt to correlate independent processing variables (e.g., screw speed, barrel temperatures, throughput, water content, and cooling temperature) with final product structure and characteristics are still the primary means of optimising the extrusion process (Emin & Schuchmann, 2017; Guyony et al., 2023; van der Sman & van der Goot, 2023; Zahari et al., 2022). The main source of these knowledge gaps, about SPC structure formation mechanisms during HME, is the lack of complementary and multiscale experimental data that could verify the proposed hypotheses.

Hence, this work focused on studying the formation of multiscale anisotropic structures during HME of a soy protein concentrate (SPC). In the interest of industrial relevance, HME was carried out on a pilot-plant scale extruder. Dead-stop experiments were performed with the aim to characterise *ex situ* the formation of multiscale structure *inside* the extruder barrel and cooling die.

The obtained HME SPC samples were studied using multiple imaging and scattering measurement techniques to cover length scales from the macro- to nano-structural level. Magnetic Resonance Imaging (MRI) has recently been shown to provide insights into phase separation in SPC extrudates (Kuijpers et al., 2024) at the μm-mm length scale range. From these high-resolution MRI images, quantitative maps of a weighted structural order parameter (WOP) could be extracted by means of the recently developed Rotated Fourier Transform (RFT) image processing method (Gobes et al., 2025). In the present work, RFT was also used to assess the coarseness of lamellar phase separation. Additionally, we mapped structural heterogeneity at mm-scale by two-dimensional scanning (Ranasinghesagara et al., 2009) of sub-mm structural anisotropy as quantified by diffuse light reflectance (DR) (Beers et al., 2017; Li et al., 2023; Ranasinghesagara et al., 2006). Measurements by means of (Ultra-)Small-Angle Scattering, of either neutrons (SANS) or X-rays ((U)SAXS), were performed to characterise nm- to μm-mm-scale structural anisotropy in SPC extrudates (Garina et al., 2024; Guan et al., 2024; Tian et al., 2020). We recently demonstrated that in SANS, the scattering contrast primarily arises from the difference in scattering length density (SLD) between soy proteins and water, while in (U)SAXS, polysaccharide fibres contribute more significantly to the signal. With the joint deployment of these two scattering measurement techniques, we can thus obtain a complementary view on structure formation of both proteins and polysaccharides, at the nm- and μm scales, in SPC high-moisture extrudates (Garina et al., 2024).

2. Materials and methods

2.1. Materials

Commercial SPC (Alpha 8® IP, 96% DM with 70% protein in dry base, 2% fat, 7% ash, 18% dietary fibre, and total carbohydrates of 19.6%) from Solae (St. Louis, MO, USA) was used in this work.

2.2. Extrusion processing

The extrusion trials were conducted on a pilot-plant scale co-rotating BCTM PolyTwin extruder from Bühler (Switzerland). The extruder had a screw diameter of 30 mm and a length-to-diameter (L/D) ratio of 40. A rectangular PolyCool 50 cooling die (Bühler, Switzerland) (Fig. S1.1 (A)) had a die opening of 60 mm × 10 mm with full bullnose edges and a length of 1200 mm, and was attached at the end of the extruder. The extruder barrel was segmented into ten temperature-controlled zones. Barrel temperatures were regulated using tempering units. The temperature in the cooling die was regulated by running water functioning as a cooling medium, and the temperature was regulated by a tempering unit. The dry protein concentrate was fed into the extruder with a solid MSDF 20 A feeder (Bühler, Switzerland). The powder was free to fall into the extruder at the first barrel through an inlet funnel. Water from the feed was heated to 80 °C and injected into the third barrel.

The extrusion trials were run at the screw speed of 300 rpm and moisture content of ca. 60%. The exact HME conditions for the dead-stop operation were selected based on the results of a design of experiments (DoE) (Box et al., 1978) as described in S2. The dead-stop operation was performed as described in Garina et al. (2024) with settings #1 in Table S2.1. Samples were taken from the extruder barrel (barrels 4, 5, 7, 9, and 10), transition, die, and cooling die zones, transferred to a watertight zip-lock bag, cooled using ice water, and then frozen for storage at −18 °C. We note that for the dead-stop samples, the moisture loss upon sampling and freeze-thawing was negligible. However, the extrudate lost approximately ∼ 10% of moisture due to steam expansion upon exiting the cooling die.

2.3. Sampling reference system

It is worth clarifying the terminology used in this work to refer to the different sample planes and positions. The sampling is generally described in Cartesian coordinates (Zink et al., 2024), where the X and Y axes represent the width and height of the cooling die, respectively, and the Z-axis represents the flow direction (Fig. 1). Consequently, there are three sample planes: sagittal (Y–Z plane), coronal (X–Z plane), and axial (X–Y plane). To account for the existing temperature gradient in the cooling die, perpendicular to the extrusion direction (Wittek, Ellwanger, et al., 2021), skin and core regions are distinguished along the Y-axis, while edge and middle regions are distinguished along the X-axis.

2.4. Diffuse light reflectance (DR)

2.4.1. DR experimental procedure

A Lumentum 1108P polarised Helium-Neon Laser with an emission wavelength of 633 nm and a beam diameter of 0.48 mm was used to obtain diffuse reflectance images. The incident light was delivered upon the sample at an angle of 70° (Fig. 1). The diffusely reflected light spot had a diameter of around 1 cm and was captured by a Mako G-234C colour camera.

2.4.2. DR image processing

The diffuse reflectance images were processed using the Halcon 21.11 software package (MVTec, Germany) and a custom-made Halcon script (Imfaimon, Barcelona, Spain) that allows for finding the major axis length ($R1$) and the minor axis length ($R2$) of a fitted ellipse. The anisotropy index (AI(DR)) was calculated as $(R1/R2)-1$. In the absence of anisotropy, AI = 0 and the light reflectance pattern is a near perfect circle. For an anisotropic sample, AI > 0.

2.4.3. 2D AI(DR) mapping

2D AI(DR) maps were obtained by moving the sample in X- or Y- direction under the laser beam, rather than using a galvanometer

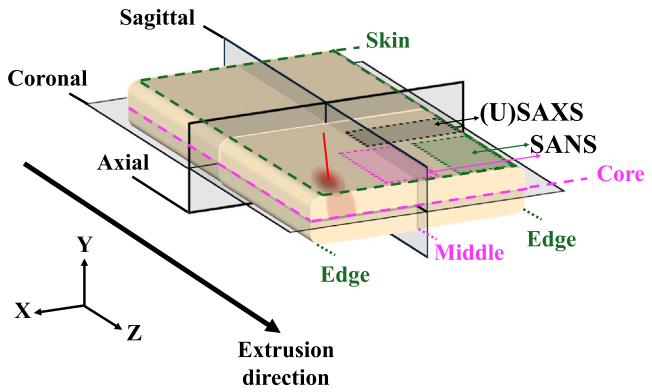

Fig. 1. The schematic representation shows the MRI slices taken, along sagittal, coronal, and axial planes and slices taken for SANS and (U)SAXS measurements of an extrudate sample (yellow volume). Skin and core regions are defined along the Y-axis. Edge and middle regions are defined along the X-axis. Additionally, the schematic illustrates the orientation of the laser beam (red spot) for diffuse reflectance measurements (red line) and its approximate penetration depth in the sample.

scanner to move the laser beam in a previous implementation (Ranasinghesagara et al., 2009). The samples were placed on a sample-bed driven by a flat gantry (DLE-FG-0001-AC-100-100 drylin®) with an X, Y travel length of 100 mm. The camera was rigidly mounted in the middle of the work area. Before each scan, the focus was adjusted once to the top surface of the sample and then kept fixed during acquisition. The exposure and lens settings were identical for all scans. The gantry itself was a toothed belt driven by an encoder with a specified repeatability of 0.5 mm (iGus, Germany). Signal conversion between programming software and gantry was done via iRC software (IGus, Germany). The sample was placed in a shallow chamber in order to position the samples in a reproducible manner. The robotic coordinates were programmed in the Igus Robot Gantry software (Igus, Germany) for the movement of the table. For every sample, an area of around 70 × 50 (Z × X; see Fig. 1) mm^2 was scanned with a step size of 2 mm in between measurements. The complete system was placed in a black box to block ambient light throughout the measurements. For every spatial coordinate, an AI(DR) value was obtained, thus yielding 2D AI(DR) maps. These maps were subdivided into three equal-size regions that are used to calculate a mean AI(DR) value for the right edge (RE), left edge (LE), and middle (M) regions of each sample (see Fig. 1).

2.5. Magnetic resonance imaging (MRI)

2.5.1. MRI sample preparation

Frozen dead-stop samples from the extruder barrel, transition zone, cooling die, and a frozen extrudate sample were swollen in demineralised water overnight at room temperature, using a water:sample weight ratio of 15:1. Swelling substantially increases ^{1}H MRI signal-to-noise ratio and the contrast between the protein-rich and water-rich phases, emphasising the lamellar structure visible by MRI (Kuijpers et al., 2024). After swelling, excess moisture was removed from the outer surface of the extrudate using a paper towel. Samples were marked on one side to identify the flow direction and orientation with respect to the extruder. Subsequently, the sample was cut into three pieces of approximately 25 mm to fit the NMR tube, and each tube was sealed with parafilm.

2.5.2. MRI experimental procedure

^{1}H MRI measurements were performed using a 600 MHz (14 T) wide-bore MRI spectrometer (Ascend 600WB Avance NEO, Bruker, Germany) equipped with a 1.5 T/m imaging gradient system (Micro 2.5, Bruker, Germany) and a 25 mm diameter quadrature dual channel ^{1}H/^{1}H detection coil (MicWB40/025 QTR, Bruker, Germany). Optimal excitation and refocusing pulse parameters were calculated by the software. Samples were measured using the Rapid Acquisition with Relaxation Enhancement (RARE) sequence (Hennig et al., 1986), which allows for shorter measurement times compared to conventional spin echo sequences. Acquisition parameters were set as follows: echo time, T_E = 10 ms; repetition time, T_R = 1 s; a RARE-factor of 2; a total of 4 averages and 5 slices recorded per image acquisition; a voxel volume of 39 × 39 × 500 μm^3; a field-of-view (FOV) of 30 × 15 mm^2 and 30 × 15.5 mm^2, respectively, for images in the sagittal and coronal plane, with a total measurement duration per image acquisition of 11 and 16 min.

2.5.3. MRI data processing

^{1}H MRI data processing and image analysis were performed in MATLAB R2022b, using the pvmatlab package from Bruker to extract the data from ParaVision 3.3. In-house scripts for automated data processing were written using either standard MATLAB functions or functions provided by the Image Processing Toolbox version 11.6 and Curve Fitting Toolbox version 3.8 from MATLAB.

2.5.4. Assessment of anisotropic structure in MRI data

RFT was used to calculate the Weighted Order Parameter (WOP) as described elsewhere (Gobes et al., 2025). RFT plugin version 0.1 was used in ImageJ (FIJI, 64-bit) version 1.54j (Schindelin et al., 2012). The images were analysed using an RFT window size of 31 px and 75% overlap between windows. Angle amplitude data were further processed using a routine (Gobes et al., 2025) written in Python 3.12, to convert the position-dependent probability of angular features into 2D spatial maps showing dominant angles, the relative angle intensity, and weighted order parameter (WOP).

The WOP(MRI) maps of the coronal images were used to assess the anisotropic structure evolution as a function of travel distance. Similarly to the AI(DR) maps, the WOP(MRI) maps were subdivided into three equal-size regions that are used to calculate a mean WOP value for the RE, LE, and M regions of each sample (see Fig. 1).

To assess the relative height of the exterior lamellar structured region ($H_{exterior}$), the sagittal WOP(MRI) maps were further processed using the following steps: (i) each WOP map was divided along the Y-direction (i.e. the sample height, see Fig. 1) into strips of four WOP values wide (Z-direction). (ii) The mean of each strip was calculated along the Z-direction and the values were inverted according to: $WOP_{inv} = 1 - WOP$, resulting in a Gaussian-shaped profile for each strip. (iii) Of these profiles, the WOP_{inv} baseline and peak value were determined and the full-width-half-maximum (FWHM) of the entire profile was calculated based on these two values. (iv) A horizontal line was projected at this FWHM value and the distance between the two points (W_{FWHM}) intersecting the WOP_{inv} profile was used to assess the height of the exterior aligned structured region according to: $H_{exterior} = W_{FWHM} - H_{sample}$. Here, H_{sample} is the height of the sample was determined from the MRI images used to calculate the WOP(MRI) maps. To correct for variations in sample height, the acquired $H_{exterior}$ is normalised to the sample height of the middle slice in the extrudate sample.

2.5.5. Assessment of lamellar structural coarseness in MRI data

The structural coarseness of the lamellar separation was quantified by determining the Weighted Characteristic Length (WCL) of the angular features. A smaller WCL value indicates a finely resolved structure, while a larger value signifies a broader separation of lamellar features. Using RFT (Gobes et al., 2025) to obtain WCL values, we analysed the data as further described in SI.4. Briefly, the procedure involves: (i) deriving a metric for the width of each angular feature, referred to as σ, using a Gaussian fit; (ii) converting σ into a wavelength using $\lambda_{px} = \frac{W}{ppw(\sigma)}$ via a calibration curve created from simulated data (ppw)

and W being the window size; and (iii) calculating an average WCL value via λ_{px} weighted by the amplitude: $WCL = \overline{\lambda_{px}}$. The assessment of statistical variation in the WCL was conducted via Multiple Linear Regression modelling (MLR) (JMP 17.2 JMP Statistical Discovery LLC.).

Additionally, to characterise the evolution of structural coarseness along the cooling die, spatial autocorrelations between neighbouring coordinates in MRI images were expressed in terms of the Global Moran's Index (I) defined as (Moran, 1950):

$$I = \frac{N}{W}\frac{\sum_i \sum_j w_{ij}(x_i - \bar{x})(x_j - \bar{x})}{\sum_i (x_i - \bar{x})^2}. \quad (1)$$

Here, N is the number of cells, x_i, j = cell of interest, $\bar{x}$ = spatial mean of x, w_{ij} = spatial weights matrix, W = sum of all w_{ij}. Calculations were performed in Matlab. An index value of −1 indicates anti-correlation between a specific cell of interest and its neighbouring cells. When the Moran's Index is zero, the cell of interest and its immediate neighbours are uncorrelated. When the Moran's Index is one, cells are clustered and thus correlated to their neighbours. Moran's I values were calculated for a neighbouring distance of 5 pixels, using line-shaped weight matrices parallel and perpendicular to the extrusion direction.

2.6. Small-angle scattering (SAS)

2.6.1. SAS sample preparation

The SAS sample preparation procedure for SAS measurements has been described in more detail elsewhere (Garina et al., 2024). Briefly, the samples were sliced along the coronal orientation (Fig. 1) at a thickness of 500 μm using a cryo-microtome (Cryostar NX70, Thermo Fisher Scientific, Germany). As shown in Fig. 1, different slices were taken from the cooling die ribbon and extrudate samples to account for the existing temperature gradient in the cooling die: separate skin edge and middle slices were prepared and measured by SANS (Section 2.6.2), and one slice covering both edge and middle regions was prepared and measured by (U)SAXS (Section 2.6.3). Only one slice was taken from the samples collected from the extruder barrel and non-cooled die zones. The acquired slices were sandwiched between microscope slides covered with Ultralene thin film (Spex® SamplePrep, USA) and subsequently sealed. This procedure ensured the stability of the product during its further storage (at −18 °C). Note that the slides and Ultralene film were removed for the following SAS measurements.

2.6.2. SANS experimental procedure and data analysis

SANS measurements were conducted on the Larmor Instrument at the ISIS Neutron and Muon Source (STFC Rutherford Appleton Laboratory, UK) (ISIS Larmor, 2023). The time-of-flight configuration of the instrument facilitated a simultaneous Q range of 0.005–0.7 Å^{-1} by employing an incident wavelength range of 0.9–13 Å. The magnitude of the momentum transfer or scattering vector, denoted as Q, is defined by the equation:

$$Q = \frac{4\pi}{\lambda}\sin\theta, \quad (2)$$

where 2θ represents the scattering angle and λ – the wavelength of the incoming neutron beam.

Given the samples' anisotropic nature, the instrument was set up using a symmetric square sample aperture (6 × 6 mm^2). The samples were placed into gel cell sample holders with demountable quartz windows to maintain an airtight environment throughout the measurements. During measurements, the samples were mounted with the specific rotation angle, ϕ_0, of 45°, as explained elsewhere (Garina et al., 2024).

The analysis of SANS data has been described in more detail elsewhere (Garina et al., 2024). Briefly, all 2D scattering data were processed using the instrument-specific software Mantid (Arnold et al., 2014). The raw data were placed on an absolute scale (cm^{-1}) by measuring the scattering of a mixture of hydrogenous and deuterated polystyrene with a known radius of gyration and scattering cross-section (Wignall & Bates, 1987). The data were corrected for detector sensitivity. The scattering background from the quartz windows was subtracted. Isotropic 2D SANS patterns were radially averaged to produce one-dimensional (1D) scattering profiles, $I(Q)$. In cases where 2D SANS data exhibited anisotropy, sector averages with a width of ±15° around the incident beam were calculated parallel (∥) and perpendicular (⊥) to the extrusion direction.

The SasView software (Doucet et al., 2022) was employed to fit both radial and sector averages of the data. The fitting process utilised a shape-independent empirical broad peak model represented by:

$$I(Q) = \frac{A}{Q^n} + \frac{C}{1 + (|Q - Q_0|\,\xi)^m} + B. \quad (3)$$

In Eq. (3), A signifies the power-law scale factor, n is the power-law exponent, C represents the Lorentzian scale factor, ξ denotes the Lorentzian correlation length, m is the exponent of Lorentz function, and B corresponds to the flat background. Q_0 is the peak position related to the characteristic centre-to-centre distance (D) between the scattering inhomogeneities, where $D = 2\pi/Q_0$.

Insights into the nano-structure anisotropy were obtained from analysing the annular intensity averages. The averaging of 2D SANS data was performed over a Q range of $Q_{min} < Q < Q_{trans}$, where Q_{min} indicates the lowest accessible scattering vector for probing the largest dimensions of the scatterers, and Q_{trans} corresponds to the transition from isotropic to anisotropic structure (Fig. 4 (left)). The resulting annular intensity averages were fitted with a Legendre series expansion (Burger et al., 2010):

$$I(Q,\phi) = \sum_{n=0}^{\infty} a_n P_{2n}(\cos\phi^*), \quad (4)$$

where $\phi^* = \phi - (\phi_0) + \frac{\pi}{2}$, ϕ_0 is the orientation angle, a_n are fitting coefficients, and P_{2n} are even Legendre polynomials. From Eq. (4), the nematic order parameter, $\overline{P_2}$, was calculated as:

$$\overline{P_2} = \frac{a_1}{5a_0}. \quad (5)$$

Here, a_0 is the isotropic (baseline) term ($P_0 = 1$), representing the mean annular intensity, and a_1 is the coefficient of the second-order Legendre polynomial $P_2(\cos\phi^*)$, which accounts for anisotropy. Thus, the value of $\overline{P_2}$ describes the degree of nano-alignment around a specific orientation angle, ϕ_0. A value closer to zero suggests a more isotropic sample, while the maximum value of the order parameter is determined by the scattering characteristics of a perfectly oriented structure.

2.6.3. (U)SAXS experimental procedure and data analysis

SAXS and USAXS measurements were performed on the upgraded beamline ID02 of the European Synchrotron Radiation Facility (ESRF, Grenoble, France) (Narayanan et al., 2022). A long evacuated detector tube allowed for automated adjustments of the sample-to-detector distance (SDD) ranging from 1 to 30.9 m, enabling the collection of SAXS and USAXS data using the same setup. For this study, three SDDs (1, 8, and 30.9 m) were used to cover a Q range of 0.0002–0.8 Å^{-1} with an X-ray wavelength of 1.014 Å.

The sample slices were positioned on the sample holder. The holder was then covered with an Ultralene film, which ensured an air-tight environment. The beam of 100 × 150 μm^2 (v × h) allowed for local examinations of different sample locations over a range of up to 28.5 mm with a step size of 0.5 mm in between measurements (the exact range was determined by the dimensions of the sample presented for the measurements), thereby covering both edge and middle regions as presented in Fig. 1.

The (U)SAXS data analysis procedure has been described in more detail in Garina et al. (2024). Accordingly, all 2D scattering data were reduced and normalised to an absolute scale (cm^{-1}) through standard procedures (Narayanan et al., 2022). The dedicated software SAXSutilities (Sztucki, 2021) was employed for scattering background

subtraction of the Ultralene film, merging measurements recorded at different SDDs and executing other specific operations. In order to account for material heterogeneity, averaging of the obtained data was performed (Garina et al., 2024). It was evaluated whether the merged intensity curves displayed characteristic shoulder-like features, or obeyed a power-law behaviour over part of the explored Q range. As for the SANS data, information regarding the structural anisotropy was derived from analysing the annular intensity averages. The annular intensity averages, $I(\phi)$, were calculated for each measurement frame. The averaging was performed over a Q range of $0.0002 < Q < 0.025$ Å^{-1} (i.e. at SDD of 30.9 m), where anisotropy was most clearly observable. The obtained annular intensity averages were fitted $I(\phi)$ with a Legendre series expansion as previously described.

3. Results and discussion

3.1. Development of μm- to mm-scale structure

Structure formation at the μm- to mm-scale during HME was investigated on samples taken from the extruder barrel, the transition zone, cooling die or the final extrudate. The samples taken from the barrel section and transition zone upon deadstop of the extruder already show lamellar structure by MRI (Fig. S1.2). This indicates that anisotropic structure formation at μm- to mm-scale is already taking place within the extruder. Example MRI and AI(DR) images for the dead-stop sample collected from the cooling die at a travel distance of 90 cm (CD 90 cm) are displayed in Fig. 2 (A). The 2D AI(DR) map, shown in Fig. 2 (A1), unveils heterogeneity in the structural anisotropy at the mm-scale. The coronal (see Fig. 1) MRI images (Fig. 2 (A2)), acquired from exactly the same sample, show this feature in the μm-mm-scale range. The areas in the RE, LE, and M regions, highlighted by rectangles in Fig. 2 (A2), were then processed using RFT to obtain the WOP(MRI) maps presented in Fig. 2 (A4). In addition, the axial (see Fig. 1) MRI image is provided in Fig. 2 (A3). We note that due to the rounded edges of the cooling die, the 2D AI(DR) map (Fig. 2 (A1)) obtained on the sample surface, does not cover the far edges of the right/left slabs captured with MRI (Fig. 2 (A2,A3) as indicated by dashed red lines. Differences in the sample areas/volumes used for AI(DR) and WOP mapping are highlighted in Fig. 2 (A3).

From inspection of Fig. 2 (A), a difference in structural anisotropy is revealed between the anisotropic edges (RE and LE) and more isotropic middle (M) regions along the X-axis, previously defined in Fig. 1. This difference in anisotropy likely arises from the larger cooling surface per volume at the rounded edges of the die, as opposed to the middle region of the die where only two cooling surfaces (Fig. 2 (A3)) are effective. Thus, due to locally faster cooling during shear, structural alignment is more pronounced towards the rounded edges, rather than in the middle region, of the cooling die. In the coronal MRI images (Fig. 2 (A2)) of this sample, two horizontal features with high signal intensities can be identified. These correspond to domains where the content, and/or the molecular mobility, of water is highest. As shown elsewhere (Kuijpers et al., 2024), these regions correspond to the positions of the twin screws in the extruder barrel.

Surprisingly, the structural anisotropy appears more pronounced at the right edge (RE, AI = 0.13) than at the left edge (LE, AI = 0.09) in the 2D AI(DR) (Fig. 2 (A1)) maps. This asymmetry can also be visually observed in the coronal and axial MRI images (Fig. 2 (A2,3)), but is not reflected in the coronal WOP(MRI) maps (Fig. 2 (A4)). We also assessed the coarseness of the lamellar structure in the coronal MRI images by quantifying the width of an angular feature (σ) in the RFT analysis via the WCL (S3.1). Here a small, but significant, difference in the coarseness of the RE and LE coronal images was found (Fig. S3.1.4). We confirmed this finding by also determining the Global Moran's I as a measure for spatial heterogeneity, which showed differences in RE and LE coronal images (Fig. S3.2.1). We attribute the RE vs LE asymmetry in AI(DR) and in the lamellar coarseness to differences in the sub-mm phase separation of the protein phase (Kuijpers et al., 2024). One possible reason for the observed asymmetry in the formation of an anisotropic phase separation could be unequal cooling of the right and left edges of the cooling die. However, the spiral design of the cooling channels in the die (see Fig. S1.1 (A)) makes it unlikely that an asymmetric temperature profile would develop across the width of the die. A more plausible explanation is that, in the absence of a breaker plate, structural heterogeneity in the protein melt, as it may have built up in the barrels and transition zone, is partially consolidated in the cooling die (Cornet et al., 2022). To verify this explanation, we repeated extrusion in the presence of a breaker plate with horizontal slots (Fig. S1.1 (B)) using processing settings comparable to settings #1 in Table S2.1. This experiment resulted in a symmetric anisotropic lamellar structure in the extrudate, as evident from axial MRI images (Fig. S1.3 (A)) and 2D AI(DR) maps (Fig. S1.3 (B)). Furthermore, the inclusion of a breaker plate also effectively erased the imprint that the two extruder screws left in the cooled samples. We conclude that the use of a breaker plate promotes a more homogeneous distribution of structure and/or temperature inside the protein melt as the latter enters the cooling die, resulting in a more homogeneous anisotropic lamellar structure formation. Without a breaker plate, a hot mass with structure and/or temperature memory enters the cooling die, where such heterogeneities are consolidated.

2D AI(DR) maps, coronal MRI images, and WOP(MRI) maps, demonstrating the evolution of anisotropic structure along the cooling die up to the obtained extrudate, are displayed in Fig. S1.4. Mean AI(DR) and mean WOP(MRI) values were calculated from the respective maps, as described in Section 2.5), the resulting plots are shown in Fig. 2 (B). As evident from Fig. 2 (B) (left), an increase is observed in AI(DR) values as a function of cooling die travel distance, with the trend being statistically significant at RE (linear regression: slope = 0.00268 per 10 cm, $p = 0.022$). However, no effect of passage over the cooling die is seen in the WOP results (Fig. 2 (B) (right)) nor in the coarseness of the phase separation quantified from the coronal MRI images (S1.4).

The sagittal MRI images (Fig. 3 (A), Fig. S1.5) reveal a lamellar structure, with an approximately parabolic shape, observed already at the beginning of the cooling die. As the material progresses through the cooling die, a region with aligned lamellae develops near the walls of the cooling die and the parabolic shape in the interior becomes more pronounced and sharp. The morphology development is seen in the WOP(MRI) maps, which in turn unveil generally increasing anisotropy in the exterior phase-separated regions (near the cooling die walls along the Y-axis and thus close to the skin, as shown in Fig. 1). The WOP(MRI) maps also show the widening of these regions during the passage of the material through the cooling die and after exiting it. This structure development was further assessed by calculating the height of the exterior lamellar structured region, as described in Section 2.5. The resulting plot is presented in Fig. 3 (B1) for the RE, M, and LE regions of the dead-stop samples, collected at increasing travel distance along the CD and after exiting it. Fig. 3 (B2) schematically shows the orientation and slice locations used to obtain these values. As seen in Fig. 3 (B1), the height of the aligned lamellar region increases in the early section of the cooling die and remains roughly unchanged as the material progressed further along the cooling die: segmented linear regression analysis indicates an early increase at M (70 cm: 0.139 mm per 10 cm, $p = 0.017$) and at LE (30 cm: 0.531 mm per 10 cm, $p = 0.023$), while downstream slopes are not statistically significant (all $p > 0.3$).

The AI(DR) and quantitative analysis of the MRI images indicate that the main effect of passage through the cooling die is the development of a layer of lamellar phase separated material near the cooled wall. The coarseness of the lamellae appears to be set by the conditions in the barrel sections and does not develop during the passage of the cooling die, which is in line with our previous study (Kuijpers et al., 2024). AI(DR) appears to be sensitive to both the size of the exterior lamellar aligned material and to its coarseness.

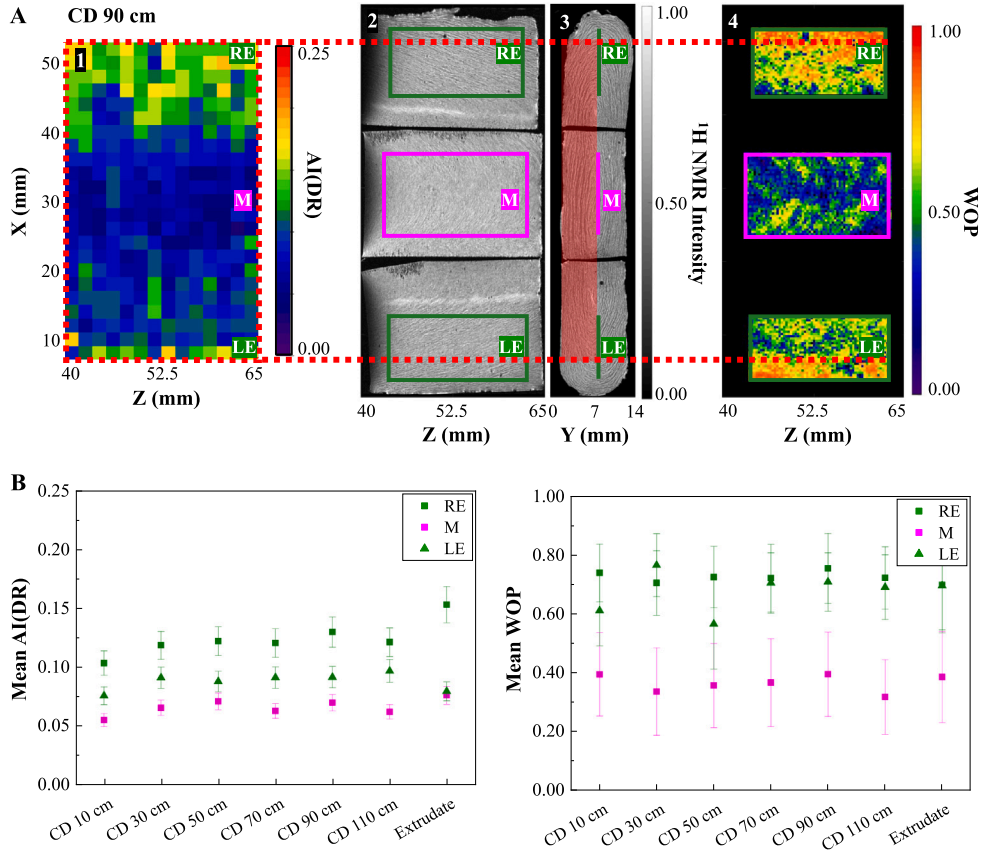

Fig. 2. (A) 2D AI(DR) maps (1), coronal and axial MRI images (2 and 3, respectively), obtained for the cooling die (CD) dead-stop sample at a travel distance of 90 cm. Areas highlighted by rectangles in (2) were further processed by RFT to obtain the WOP map in (4). The red rectangle in (3) schematically demonstrates the volume sampled by 2D AI(DR). The green and magenta lines in (3) refer to the location of the RFT analysed sample volumes taken to obtain the coronal WOP maps. (B) Structural evolution along the cooling die is characterised by plotting the mean AI(DR) (left) and mean WOP (right) calculated from the respective 2D AI(DR) and coronal WOP maps of CD dead-stop and extrudate samples (Fig. S1.4).

3.2. Development of nm- to μm *structure*

3.2.1. Small-angle neutron scattering (SANS)

To obtain insights into the structure formation at the nm-μm scale, SAS measurements were performed on the extrudate and dead-stop samples collected from the barrel, transition, non-cooled die, and cooling die zones.

Since HME induces a preferred orientation along the flow direction, 2D SANS data were averaged in 30°-wide sectors around the incident beam in the directions parallel and perpendicular to the orientation direction. From Fig. 4 (left), it is evident that protein structures in the extrudates are aligned already at length scales above ca. 20 nm. This finding is in agreement with previous observations of alignment of calcium caseinate fibrils in sheared gels at similar length scales (Tian et al., 2020). Furthermore, formation of fibril structures consisting of highly compacted ultra-thin filaments with a thickness of 20–30 nm has been observed in soy protein extrudates (Chiang et al., 2021; Zink et al., 2024).

A distinctive shoulder-like feature is observed in the Q range between ca. 0.015 and 0.065 Å^{-1}. The empirical broad peak model provides a good fit along the entire Q range and reproduces this shoulder feature. The fit allows for determining the characteristic sizes of the nanostructures present in the material. In Zink et al. (2024), the peak position (Q_0) was attributed to the main average centre-to-centre distance (D) between agglomerated proteins, connected by electrostatic or covalent forces, to form the fibrous structure of meat alternatives. Fig. 4 (right) shows that D remains roughly unchanged along the extruder barrel and the entire cooling die section. The same observation was made in our previous work (Garina et al., 2024), where sampling of the screw section was performed at the final extruder barrel section of a lab-scale extruder. In the current work, the use of a larger scale pilot-plant extruder allowed samples to be collected from earlier screw sections. The obtained results imply that the equilibrium size protein aggregate building blocks are already formed in the beginning sections of the extruder barrel. Considering that the barrel 4 (B4) sample was taken from the barrel section at $T > 120$ °C (Table S2.1 #1), the data are consistent with the hypothesised protein aggregation mechanism proposed earlier by van der Sman and van der Goot (2023): protein aggregates grow in the screw sections at 90 °C < T < 120 °C and are subsequently size-limited by shear induced fragmentation at $T > 120$ °C, resulting in shear-resistant aggregates that act as fibrillar building blocks.

The broad peak model fit also provides the Lorentzian correlation length (ξ) (Table S1.1), defined as the size of the smallest discernible scattering object (Tian et al., 2020). Similar to the centre-to-centre distance, it does not change along the extruder or the entire cooling die. A ξ of ca. 10 nm seems to be close to the diameter of native glycinin and β-conglycinin molecules, the two major globulins in soy storage proteins (Badley et al., 1975). This finding would imply that the building blocks of protein fibrils are constituted from moderately unfolded but still globular proteins; under HME conditions protein most likely behave as globular polymers rather than random-coil chains (Guan et al., 2024). Preservation of the globular shapes of proteins and their aggregation during heat treatment was also shown in Nakamura et al. (1984) and in Guan et al. (2024), where similar ξ values were obtained from SANS data.

The extent of alignment of the protein fibrils was quantified by fitting the annular intensity averages with the Legendre series

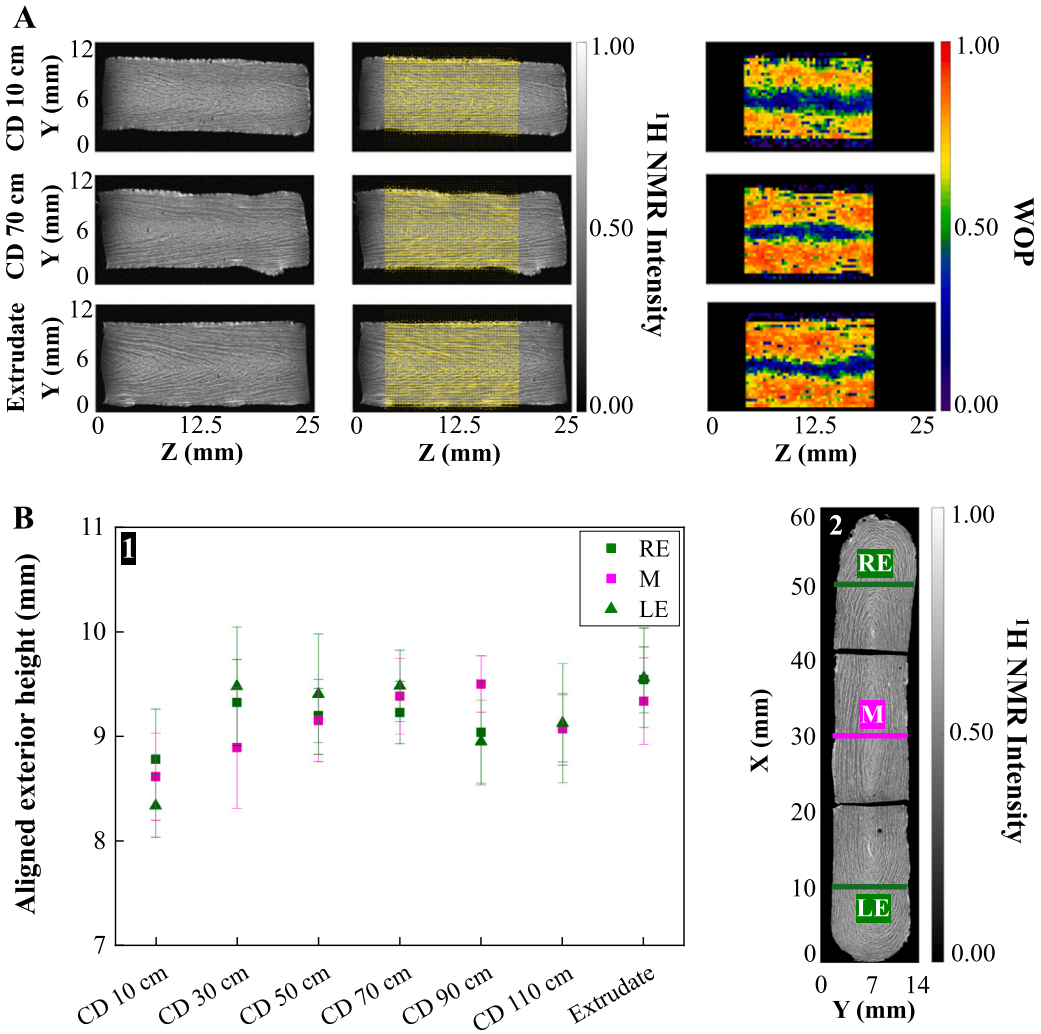

Fig. 3. (A) Selected sagittal MRI images without (left) or with (centre) overlaid angle distribution map (yellow lines), and WOP(MRI) maps (right) for the dead-stop SPC samples collected at increasing distance, from top to bottom, within the cooling die (CD). The bottommost row refers to an SPC extrudate sample. (B) (1) Structural evolution demonstrated by the height of the exterior aligned lamellar structure calculated from the WOP maps of the sagittal MRI images of CD dead-stop and extrudate samples. (2) Axial MRI image demonstrating schematically the orientation and slice locations used to obtain these values.

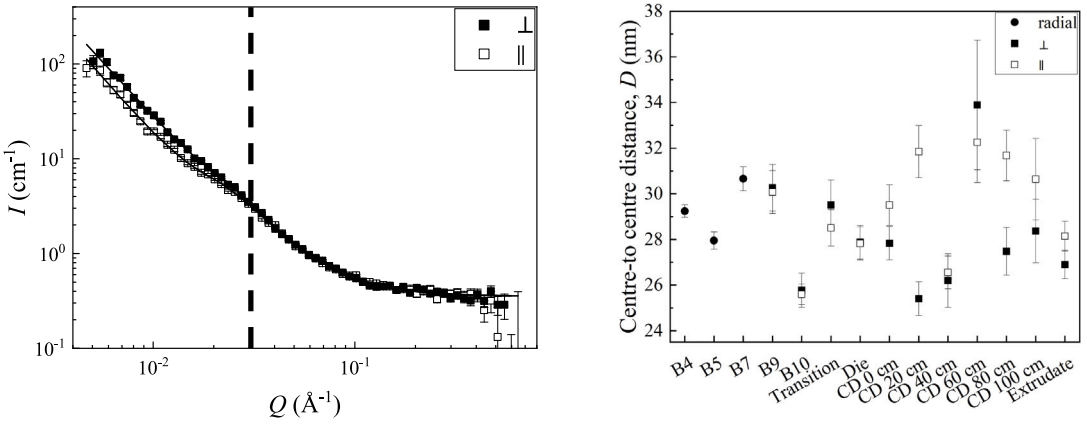

Fig. 4. (Left): Sector averages of 2D SANS data taken in the directions parallel (‖) and perpendicular (⊥) to the orientation direction for the extrudate skin edge slices. Square symbols represent the experimental data and lines represent the fit with the broad peak model. The vertical dashed line indicates the transition between isotropic and anisotropic structures. (Right): Centre-to-centre distances between scattering inhomogeneities (protein aggregates) estimated from the broad peak model for the extrudate and dead-stop samples collected from barrel (B), transition, non-cooled die, and cooling die (CD) zones. Since the 2D data from barrels 4, 5, and 7 displayed no anisotropy, radially averaged intensities were fitted with the model (circle symbols). For the other dead-stop and extrudate samples, sector intensities were used for the fit (square symbols). Note that for clarity, the data from the cooling die and extrudate samples are shown for (right) edge slices only. All fitting parameters are presented in Table S1.1.

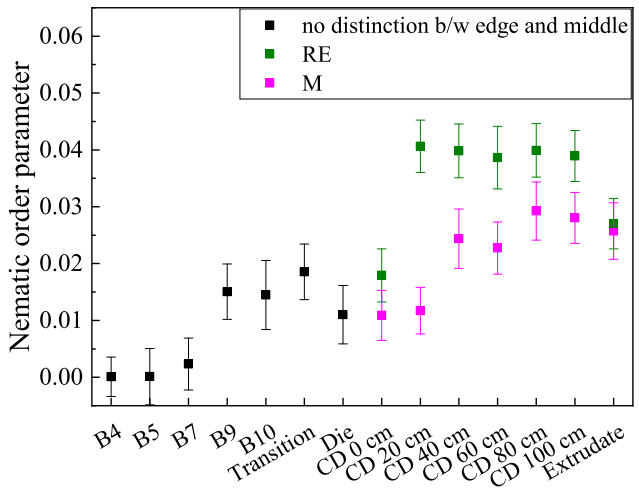

Fig. 5. Nematic order parameter (Eq. (5)) calculated from SANS measurements of SPC ribbon samples from a dead-stop experiment, collected within the barrel (B) section, the transition region or the cooling die (CD), as well as of an SPC extrudate. Green and magenta symbols, respectively, refer to exterior (RE) and interior (M) regions of the CD samples, affected by the temperature gradient inside the cooling die (for reference, see Fig. 1). In the other zones (black symbols), there is no such temperature gradient, so no distinction was made between the regions during sampling.

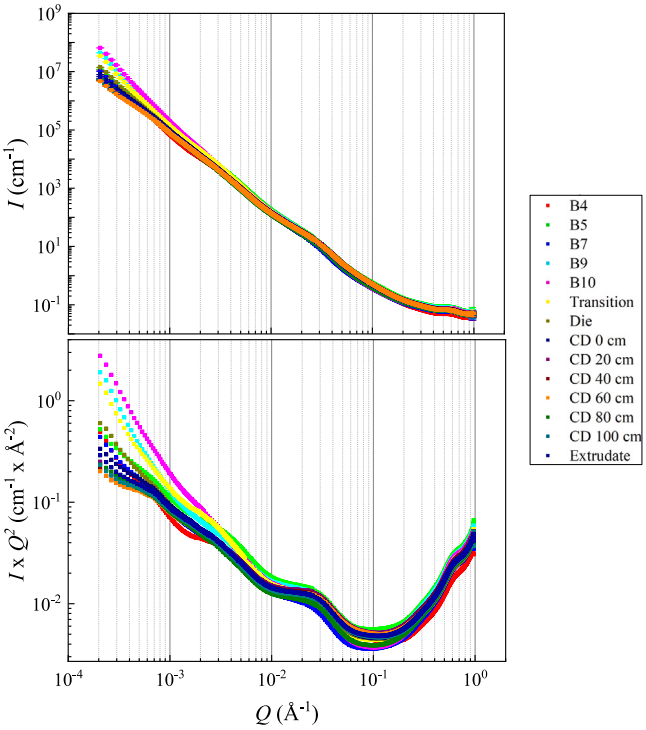

Fig. 6. Radially averaged (U)SAXS data additionally averaged over all measurement frames (top); corresponding Kratky plots (bottom). Data were obtained by combining three SDDs.

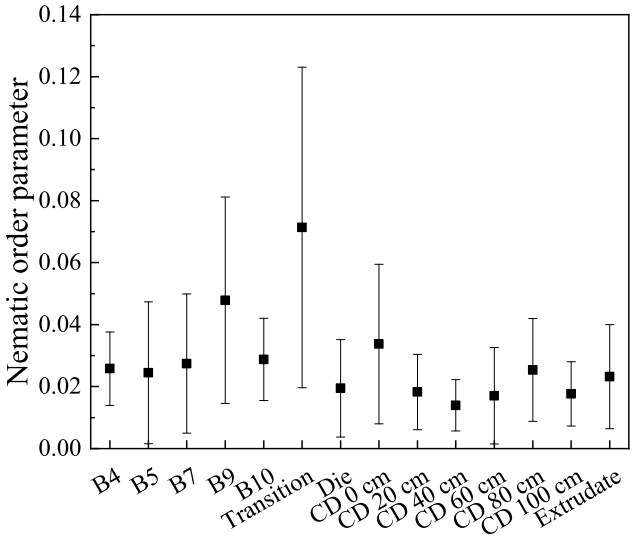

Fig. 7. Nano- and microstructure evolution during HME demonstrated by nematic order parameters (Eq. (5)) calculated from USAXS data at SDD of 31 m, i.e., at length scales of ca. 30 nm - 3 μm. Plotted values are the means across several measurement frames taken along a single transverse scan from the RE toward the interior (Fig. 1).

expansion, as described in Section 2.6.2. Fig. 5 displays the calculated nematic order parameter that describes nano-anisotropy evolution at ca. 20–125 nm. Note that the edge slices for the SAS measurements were taken only from the right edge that demonstrated more anisotropy, as determined by DR (Fig. 2). The results indicate that the anisotropic structure is already formed before the melt arrives at the cooling die section in line with the hypothesis proposed by van der Sman and van der Goot (2023). When the protein melt enters the cooling die, this anisotropic fibrillar aggregation is emphasised by the cooling and subsequent solidification of the protein network, and driven further by the shear forces generated therein (Cornet et al., 2022; van der Sman & van der Goot, 2023; Wittek, Ellwanger, et al., 2021).

Interestingly, our previous work (Garina et al., 2024) showed only marginal change in the SANS nematic order parameter when the material entered the short cooling die of a lab-scale extruder. In the present work, however, we observe a drastic increase in the protein nanoscale nematic order in the early section of the cooling die, which is also in line with the results on the height of the exterior aligned region in Fig. 3 (B1). We note that the temperatures of the protein melt, when entering the cooling dies of the lab- and pilot-plant extruders (T = 141 °C and$T$ = 127 °C, respectively), as well as the respective dosed moisture contents (54% and 60%), are different. Our current explanation is that the higher moisture content used in our pilot-plant extruder trial led to a less viscous protein melt entering the cooling die. This allowed for a further increase in the protein nanoscale nematic order in the first section of the cooling die.

Similarly to the 2D AI(DR) and WOP(MRI) results, the nematic order parameter, which describes anisotropy at the nanoscale, demonstrates the difference between the anisotropic edge and the isotropic middle region (Fig. 5) and is also visible from the confocal laser scanning microscopy (CLSM) images (Fig. S1.6 (G,H)). Consistency in the results obtained from SANS, MRI and DR suggests that there is a connection between fibrillation aggregation at the nm-μm scale and phase separation at the μm-mm scale. Therefore, we adhere to the hypothesis proposed by van der Sman and van der Goot (2023), which suggests that phase separation occurs due to the contraction of the cross-linked protein matrix. Our previous research (Kuijpers et al., 2025) indicated that this contraction is likely the consequence of the formation of a fibrillar protein network, whereby the presence or absence of anisotropic fibrillar protein aggregation appears to determine whether phase separation is lamellar or isotropic.

3.2.2. (Ultra-)small-angle X-ray scattering ((U)SAXS)

As explained in Section 2.6.3, SAXS and USAXS measurements were performed on different sample spots over a distance of up to 28.5 mm

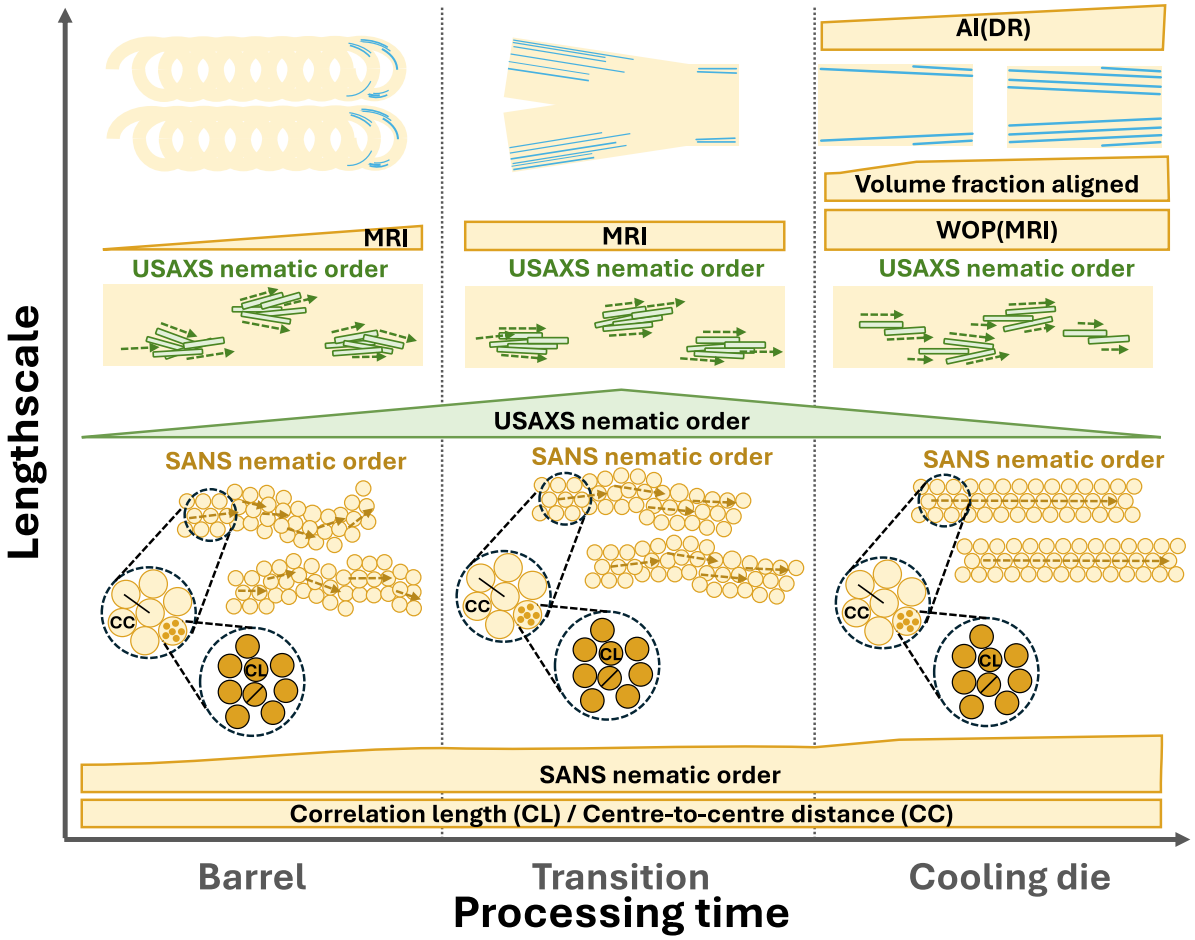

Fig. 8. Schematic diagram reflecting multiscale structure formation in HME at: the mm scale, as probed by 2D AI(DR); the sub-mm scale, as probed by MRI-WOP; the nm- and sub-μm scale, as probed by SAS.

along X-axis (see Fig. 1). In order to observe structural evolution along the extruder barrel and cooling die sections, averaging over all measurement frames was performed. An example of the integrated scattering curves of all sample positions along the cooling die width is shown in Fig. S1.7. The resulting scattering profiles are displayed in Fig. 6.

Similarly to the SANS data, a shoulder-like feature is evident in the Q range between ca. 0.01 and 0.07 Å^{-1} and, therefore, attributed to protein aggregate building blocks. In SANS data, the higher-Q range (Q > 0.07 Å^{-1}) was dominated by incoherent background scattering (Fig. 4 (left)), but in SAXS data, an additional shoulder-like feature becomes distinguishable (Fig. 6 (top)). This feature is related to a real-space position of ca. 1 nm (Q of ca. 0.6 Å^{-1}) and, therefore, might correspond to the inter-β-sheet distance (Zink et al., 2024). The presence of additional shoulder features is detected in the lower-Q region, which was not achievable with SANS (Q < 0.005 Å^{-1}). In Garina et al. (2024), Zink et al. (2024), the shoulder in the Q range between ca. 0.002 and 0.007 Å^{-1}, corresponding to real-space distances of ca. 90–315 nm, was attributed to fibrillar structures of proteins. Furthermore, scattering intensities of all samples display an additional shoulder in the Q range between ca. 0.0004 and 0.0008 Å^{-1}. However, this feature is less pronounced in the extruder barrel and transition zone samples, where the lowest Q region (Q < 0.001 Å^{-1}) seems to be more dominated by the power-law compared to the cooling die. In Garina et al. (2024), this was attributed to the presence of more clustered or densely packed polysaccharide fibres in the extruder barrel, which undergo deformation and distribute more homogeneously in the cooling die.

Consistent with our SAXS results reported previously (Garina et al., 2024), all shoulder positions in SAXS profiles remain roughly unchanged with the sample's position along the extruder barrel or cooling die. This implies that, starting from barrel 4 (T > 120 °C), proteins do not undergo clear conformational changes, as indicated by the steady shoulder at ca. 1 nm. These proteins assemble into aggregates of the equilibrium size, as described in Section 3.2.1, and constitute the nanoscale building blocks of protein fibrils, which in turn seem to be formed already in the first barrel zones at T > 120 °C. CLSM results support these observations and demonstrate the presence of protein fibrils along the entire extruder barrel section (Fig. S1.6).

Interestingly, in contrast to the SANS results (Fig. 5), the nematic order parameter determined from USAXS data shows the highest alignment in the transition zone (Fig. 7) (for statistical analysis, see Tables S1.2 and S1.3). We note that since the calculated values varied significantly at different sample locations along X-axis (Fig. S1.8), Fig. 7 displays the mean nematic order parameter across several measurement frames. In Garina et al. (2024), these differences between the SANS and (U)SAXS results were explained by a contrast difference in SLD encountered for proteins and polysaccharide fibres. In SANS, the scattering contrast arises primarily from the SLD difference of soy proteins relative to water, accordingly, the SANS nematic order parameter reflects protein alignment. Even though it is impossible to completely separate the contributions of these two biopolymers, it is still clear that dispersed polysaccharide fibres, originating from cell wall fragments, contribute more to (U)SAXS than to SANS. It is this contribution of cell wall fragments that appears to be responsible for the strongest local alignment observed in the transition zone, where tensile stresses are the

highest. Despite the apparent structural relaxation in the cooling die, an increase in the extent of alignment closer to the cooling die walls along the X-axis is still evident, as shown in Fig. S1.8. These observations are in agreement with the SANS results showing stronger alignment in the sample edge compared to the middle (Fig. 5).

4. Conclusions

This work has demonstrated how multiscale structure, probed from the nano- to the macro scale, evolves during pilot-plant HME. Fig. 8 schematically reflects this multiscale structure development.

The mm-scale heterogeneity in structural anisotropy is described by 2D AI(DR) maps (Fig. 8 (top right)). The monotonic development of structural anisotropy is evident as the material progresses through the cooling die. Perpendicular to the flow direction we observed more structural anisotropy at the edges where more cooling surface per volume is present. MRI showed that local μm- to mm-scale alignment is already present at the end of the barrel and in the transition zone, with substantial lamellar alignment found at the beginning of the cooling die (Fig. 8 (top)). The height of the structured lamellar region increases in the early sections of the cooling die, whereas no effect of the passage over the cooling die is found for WOP(MRI) and coarseness of the lamellar phase-separation. AI(DR) and MRI showed that in the absence of a breaker plate coarseness of the sub-mm lamellar structure is asymmetric perpendicular to the extrusion direction. In the presence of a breaker plate, these and other structural heterogeneities are absent, indicating a homogeneous structure and/or temperature distribution of the protein melt as it enters the cooling die. The local USAXS order parameter (Fig. 8 (middle)) describes the alignment of polysaccharide fibres and reaches its maximum in the transition zone where the tensile stresses are highest. The SANS nematic order parameter (Fig. 8 (middle)), in turn, describes the alignment of protein fibrils, and shows that the nm-scale anisotropic protein structure is formed already in the extruder barrel, and further develops in the early sections of the cooling die. The protein fibrils are shown to be formed from the protein aggregate building blocks with a characteristic centre-to-centre distance (CC in Fig. 8 (bottom)), which are constituted from moderately unfolded, yet globular, proteins with a characteristic correlation length (CL in Fig. 8 (bottom)). Both CC distance and CL remain roughly unchanged as the protein melt progresses through the extruder barrel to the cooling die.

The deployment of imaging and scattering measuring modalities, as discussed in this work, provides a comprehensive view on the structural events occurring during HME at pilot-plant scale. We foresee further deployment of these techniques in establishing mechanistic links between the events that occur during HME at different length scales. For this purpose we envisage future *in situ* characterisation of structure formation by both MRI velocimetry and SAS measurements during HME.

CRediT authorship contribution statement

Ekaterina D. Garina: Writing – original draft, Visualization, Methodology, Investigation, Formal analysis, Data curation, Conceptualization. **Sam A. Kuijpers:** Writing – review & editing, Visualization, Methodology, Investigation, Formal analysis, Data curation, Conceptualization. **Martijn I. Gobes:** Writing – review & editing, Software, Methodology, Formal analysis, Data curation, Conceptualization. **Arjen Sein:** Writing – review & editing, Resources, Methodology. **Ruud den Adel:** Methodology. **Gregory N. Smith:** Writing – review & editing, Software, Formal analysis, Data curation. **Michael Sztucki:** Writing – review & editing, Software, Formal analysis, Data curation. **Johannes Hohlbein:** Writing – review & editing, Supervision, Conceptualization. **Camilla Terenzi:** Writing – review & editing, Supervision, Project administration, Funding acquisition, Conceptualization. **John P.M. van Duynhoven:** Writing – review & editing, Supervision, Resources, Funding acquisition, Conceptualization. **Wim G. Bouwman:** Writing – review & editing, Supervision, Funding acquisition, Conceptualization.

Declaration of competing interest

The authors declare the following financial interests/personal relationships which may be considered as potential competing interests: John P.M. van Duynhoven and Ruud den Adel are employed by a company that manufactures and markets plant-based meat alternatives. Arjen Sein is employed by a company that sells plant-based ingredients. The other authors declare that they have no known competing financial interests or personal relationships that could have appeared to influence the work reported in this paper.

Acknowledgements

This work is part of the project “Measurement and Modelling of Multiscale Processed Protein Products (MP3)” (with project number 18744) of the research programme OPT TTW, which is financed by the Dutch Research Council as well as by contributions from consortium partners Unilever, Cargill, United States, dsm-firmenich, FrieslandCampina and Wageningen Food and Biobased Research. We gratefully acknowledge the Science and Technology Facilities Council (STFC) for access to neutron beamtime at ISIS through RB 2369100 (data are available at https://doi.org/10.5286/ISIS.E.RB2369100). We also acknowledge the European Synchrotron Radiation Facility (ESRF) for the provision of synchrotron radiation facilities (data are available at https://doi.org/10.5281/zenodo.14651762). This project was further supported by the uNMR-NL Grid: A distributed, state-of-the-art Magnetic Resonance facility for the Netherlands (NWO grant 184.035.002). This work benefited from the use of the SasView application, originally developed under NSF Award DMR-0520547. SasView also contains code developed with funding from the EU Horizon 2020 programme under the SINE2020 project Grant No. 654000. Unilever is thanked for the use of the 2D AI(DR) instrument. Eduard Mooy and Remon Lippens are thanked for skillfully constructing this instrument. Finally, we thank the dsm-firmenich Extrusion Test Center in Tau (Norway) for access to the pilot-plant extruder and Tore Stendahl and Bolor Borjgen for their support during extrusion trials.

Appendix A. Supplementary data

Supplementary material related to this article can be found online at https://doi.org/10.1016/j.foodhyd.2025.112037.

Data availability

SANS data are available at https://doi.org/10.5286/ISIS.E.RB2369100. (U)SAXS data are available at https://doi.org/10.5281/zenodo.14651762.

References

Akdogan, H. (1999). High moisture food extrusion. *International Journal of Food Science & Technology*, *34*(3), 195–207. http://dx.doi.org/10.1046/j.1365-2621.1999.00256.x.

Andreani, G., Sogari, G., Marti, A., Froldi, F., Dagevos, H., & Martini, D. (2023). Plant-based meat alternatives: Technological, nutritional, environmental, market, and social challenges and opportunities. *Nutrients*, *15*(2), 452. http://dx.doi.org/10.3390/nu15020452.

Arnold, O., Bilheux, J. C., Borreguero, J. M., Buts, A., Campbell, S. I., Chapon, L., Doucet, M., Draper, N., Ferraz Leal, R., Gigg, M. A., Lynch, V. E., Markvardsen, A., Mikkelson, D. J., Mikkelson, R. L., Miller, R., Palmen, K., Parker, P., Passos, G., Perring, T. G., ... Zikovsky, J. (2014). Mantid - data analysis and visualization package for neutron scattering and μ SR experiments. *Nuclear Instruments and Methods in Physics Research, Section A: Accelerators, Spectrometers, Detectors and Associated Equipment*, *764*, 156–166. http://dx.doi.org/10.1016/j.nima.2014.07.029.

Badley, R. A., Atkinson, D., Hauser, H., Oldani, D., Green, J. P., & Stubbs, J. M. (1975). The structure, physical and chemical properties of the soy bean protein glycinin. *Biochimica Et Biophysica Acta (BBA) - Protein Structure*, *412*(2), 214–228. http://dx.doi.org/10.1016/0005-2795(75)90036-7.

Beers, R. V., Saeys, W., Reis, M. M., & Aernouts, B. (2017). Anisotropic light propagation in bovine muscle tissue depends on the initial fiber orientation, muscle type and wavelength. *Optics Express*, *25*(18), 22082–22095. http://dx.doi.org/10.1364/OE.25.022082.

Beniwal, A. S., Singh, J., Kaur, L., Hardacre, A., & Singh, H. (2021). Meat analogs: Protein restructuring during thermomechanical processing. *Comprehensive Reviews in Food Science and Food Safety*, *20*(2), 1221–1249. http://dx.doi.org/10.1111/1541-4337.12721.

Bonnet, C., Bouamra-Mechemache, Z., Réquillart, V., & Treich, N. (2020). Viewpoint: Regulating meat consumption to improve health, the environment and animal welfare. *Food Policy*, *97*, Article 101847. http://dx.doi.org/10.1016/j.foodpol.2020.101847.

Box, G., Hunter, W., & Hunter, S. (1978). *Statistics for experimenters*.

Burger, C., Hsiao, B. S., & Chu, B. (2010). Preferred orientation in polymer fiber scattering. *Polymer Reviews*, *50*(1), 91–111. http://dx.doi.org/10.1080/15583720903503494.

Chiang, J. H., Tay, W., Ong, D. S. M., Liebl, D., Ng, C. P., & Henry, C. J. (2021). Physicochemical, textural and structural characteristics of wheat gluten-soy protein composited meat analogues prepared with the mechanical elongation method. *Food Structure*, *28*, Article 100183. http://dx.doi.org/10.1016/j.foostr.2021.100183.

Cornet, S. H., Snel, S. J., Schreuders, F. K., van der Sman, R. G., Beyrer, M., & van der Goot, A. J. (2022). Thermo-mechanical processing of plant proteins using shear cell and high-moisture extrusion cooking. *Critical Reviews in Food Science and Nutrition*, *62*(12), 3264–3280. http://dx.doi.org/10.1080/10408398.2020.1864618.

Dekkers, B. L., Boom, R. M., & van der Goot, A. J. (2018). Structuring processes for meat analogues. *Trends in Food Science & Technology*, *81*, 25–36. http://dx.doi.org/10.1016/j.tifs.2018.08.011.

Doucet, M., Cho, J. H., Alina, G., Attala, Z., Bakker, J., Bouwman, W., Bourne, R., Butler, P., Cadwallader-Jones, I., Campbell, K., Cooper-Benun, T., Durniak, C., Forster, L., Gilbert, P., Gonzalez, M., Heenan, R., Jackson, A., King, S., Kienzle, P., ... Wolf, C. (2022). SasView version 5.0.5. http://dx.doi.org/10.5281/zenodo.6331344.

Emin, M. A., & Schuchmann, H. P. (2017). A mechanistic approach to analyze extrusion processing of biopolymers by numerical, rheological, and optical methods. *Trends in Food Science & Technology*, *60*, 88–95. http://dx.doi.org/10.1016/j.tifs.2016.10.003.

Garina, E. D., den Adel, R., van Duynhoven, J. P., Smith, G. N., Dalgliesh, R. M., Sztucki, M., & Bouwman, W. G. (2024). SANS and SAXS: A Love story to unravel structural evolution of soy proteins and polysaccharide fibres during high moisture extrusion for meat alternatives. *Food Hydrocolloids*, *155*, Article 110121. http://dx.doi.org/10.1016/j.foodhyd.2024.110121.

Gobes, M. I., Kuijpers, S. A., Terenzi, C., van der Sman, R. G., van Duynhoven, J. P., & Hohlbein, J. (2025). Rotated Fourier transform (RFT) enables the quantification of anisotropic structure in high-moisture plant-protein extrudates. *Food Structure*, *44*, Article 100437. http://dx.doi.org/10.1016/j.foostr.2025.100437.

González, N., Marquès, M., Nadal, M., & Domingo, J. L. (2020). Meat consumption: Which are the current global risks? A review of recent (2010–2020) evidences. *Food Research International*, *137*, Article 109341. http://dx.doi.org/10.1016/j.foodres.2020.109341.

Guan, T., Sägesser, C., Villiger, R., Zychowski, L., Kohlbrecher, J., Dumpler, J., Mathys, A., Rühs, P., Fischer, P., & Matsarskaia, O. (2024). In situ studies of plant-based meat analog texturization. *Food Hydrocolloids*, *155*, Article 110215. http://dx.doi.org/10.1016/j.foodhyd.2024.110215.

Guyony, V., Fayolle, F., & Jury, V. (2023). High moisture extrusion of vegetable proteins for making fibrous meat analogs: A review. *Food Reviews International*, *39*(7), 4262–4287. http://dx.doi.org/10.1080/87559129.2021.2023816.

He, J., Evans, N. M., Liu, H., & Shao, S. (2020). A review of research on plant-based meat alternatives: Driving forces, history, manufacturing, and consumer attitudes. *Comprehensive Reviews in Food Science and Food Safety*, *19*, 2639–2656. http://dx.doi.org/10.1111/1541-4337.12610.

Hennig, J., Nauerth, A., & Friedburg, H. (1986). RARE imaging: A fast imaging method for clinical MR. *Magnetic Resonance in Medicine*, *3*(6), 823–833. http://dx.doi.org/10.1002/mrm.1910030602.

ISIS Larmor (2023). https://www.isis.stfc.ac.uk/Pages/Larmor.aspx. [Accessed 21 July 2023].

Kaunisto, E., Wassén, S., & Stading, M. (2024). A thermodynamical finite element model of the fibre formation process during extrusion of high-moisture meat analogues. *Journal of Food Engineering*, *362*, Article 111760. http://dx.doi.org/10.1016/j.jfoodeng.2023.111760.

Kuijpers, S. A., Garina, E. D., Gobes, M. I., den Adel, R., Smith, G. N., Sztucki, M., Hohlbein, J., Bouwman, W. G., van Duynhoven, J. P., & Terenzi, C. (2025). Impact of pH-shifting on multiscale structural anisotropy of high-moisture extrudates of soy proteins. *Food Hydrocolloids*, *168*, Article 111456. http://dx.doi.org/10.1016/j.foodhyd.2025.111456.

Kuijpers, S. A., Goudappel, G.-J., Huppertz, T., van Duynhoven, J. P., & Terenzi, C. (2024). Quantification of phase separation in high moisture soy protein extrudates by NMR and MRI. *Food Research International*, *197*, Article 115225. http://dx.doi.org/10.1016/j.foodres.2024.115225.

Li, J., Xia, X., Shi, C., Chen, X., Tang, H., & Deng, L. (2023). A reliable method for determining the degree of orientation of fibrous foods using laser transmission and computer vision. *Foods*, *12*(19), 3541. http://dx.doi.org/10.3390/foods12193541.

Moran, P. (1950). Notes on continuous stochastic phenomena. *Biometrika*, *37*(1), 17–23. http://dx.doi.org/10.2307/2332142.

Nakamura, T., Utsumi, S., & Mori, T. (1984). Network structure formation in thermally induced gelation of glycinin. *Journal of Agricultural and Food Chemistry*, *32*(2), 349–352. http://dx.doi.org/10.1021/jf00122a042.

Narayanan, T., Sztucki, M., Zinn, T., Kieffer, J., Homs-Puron, A., Gorini, J., Van Vaerenbergh, P., & Boesecke, P. (2022). Performance of the time-resolved ultra-small-angle X-ray scattering beamline with the extremely brilliant source. *Journal of Applied Crystallography*, *55*(1), 98–111. http://dx.doi.org/10.1107/S1600576721012693.

Ranasinghesagara, J., Hsieh, F.-H., Huff, H., & Yao, G. (2009). Laser scanning system for real-time mapping of fiber formations in meat analogues. *Journal of Food Science*, *74*(2), E39–E45. http://dx.doi.org/10.1111/j.1750-3841.2008.01032.x.

Ranasinghesagara, J., Hsieh, F., & Yao, G. (2006). A photon migration method for characterizing fiber formation in meat analogs. *Journal of Food Science*, *71*(5), E227–E231. http://dx.doi.org/10.1111/j.1750-3841.2006.00038.x.

Sandoval Murillo, J. L., Osen, R., Hiermaier, S., & Ganzenmüller, G. (2019). Towards understanding the mechanism of fibrous texture formation during high-moisture extrusion of meat substitutes. *Journal of Food Engineering*, *242*, 8–20. http://dx.doi.org/10.1016/j.jfoodeng.2018.08.009.

Schindelin, J., Arganda-Carreras, I., Frise, E., Kaynig, V., Longair, M., Pietzsch, T., Preibisch, S., Rueden, C., Saalfeld, S., Schmid, B., Tinevez, J. Y., White, D. J., Hartenstein, V., Eliceiri, K., Tomancak, P., & Cardona, A. (2012). Fiji: an open-source platform for biological-image analysis. *Nature Methods*, *9*, 676–682. http://dx.doi.org/10.1038/nmeth.2019.

Sztucki, M. (2021). SAXSutilities: a graphical user interface for processing and analysis of small-angle X-ray scattering data (1.024). http://dx.doi.org/10.5281/zenodo.5825707.

Tian, B., Wang, Z., de Campo, L., Gilbert, E. P., Dalgliesh, R. M., Velichko, E., van der Goot, A. J., & Bouwman, W. G. (2020). Small angle neutron scattering quantifies the hierarchical structure in fibrous calcium caseinate. *Food Hydrocolloids*, *106*, Article 105912. http://dx.doi.org/10.1016/j.foodhyd.2020.105912.

Tolstoguzov, V. B. (1993). Thermoplastic extrusion—the mechanism of the formation of extrudate structure and properties. *Journal of the American Oil Chemists' Society*, *70*(4), 417–424. http://dx.doi.org/10.1007/BF02552717.

van der Sman, R. G., & van der Goot, A. J. (2023). Hypotheses concerning structuring of extruded meat analogs. *Current Research in Food Science*, *6*, Article 100510. http://dx.doi.org/10.1016/j.crfs.2023.100510.

Wang, Y., Lyu, B., Fu, H., Li, J., Ji, L., Gong, H., Zhang, R., Liu, J., & Yu, H. (2023). The development process of plant-based meat alternatives: Raw material formulations and processing strategies. *Food Research International*, *167*, Article 112689. http://dx.doi.org/10.1016/j.foodres.2023.112689.

Wignall, G. D., & Bates, F. S. (1987). Absolute calibration of small-angle neutron scattering data. *Journal of Applied Crystallography*, *20*(1), 28–40. http://dx.doi.org/10.1107/S0021889887087181.

Wittek, P., Ellwanger, F., Karbstein, H. P., & Emin, M. A. (2021). Morphology development and flow characteristics during high moisture extrusion of a plant-based meat analogue. *Foods*, *10*(8), 1753. http://dx.doi.org/10.3390/foods10081753.

Wittek, P., Zeiler, N., Karbstein, H. P., & Emin, M. A. (2021). High moisture extrusion of soy protein: Investigations on the formation of anisotropic product structure. *Foods*, *10*(1), 102. http://dx.doi.org/10.3390/foods10010102.

Zahari, I., Östbring, K., Purhagen, J. K., & Rayner, M. (2022). Plant-based meat analogues from alternative protein: A systematic literature review. *Foods*, *11*(18), 2870. http://dx.doi.org/10.3390/foods11182870.

Zink, J. I., Lutz-Bueno, V., Handschin, S., Dütsch, C., Diaz, A., Fischer, P., & Windhab, E. J. (2024). Structural and mechanical anisotropy in plant-based meat analogues. *Food Research International*, *179*, Article 113968. http://dx.doi.org/10.1016/j.foodres.2024.113968.